Manganese-hydrogen complexes in $Ga_{1-x}Mn_xN$

C. Bihler,[1,*] U. Gerstmann,[2,3] M. Hoeb,[1] T. Graf,[1] M. Gjukic,[1] W. G. Schmidt,[3] M. Stutzmann,[1] and M. S. Brandt[1]
[1]*Walter Schottky Institut, Technische Universität München, Am Coulombwall 3, 85748 Garching, Germany*
[2]*Institut de Minéralogie et Physique des Milieux Condensés, Université Pierre et Marie Curie, Campus Boucicaut, 140 rue de Lourmel, 75015 Paris, France*
[3]*Department Physik, Universität Paderborn, Warburger Str. 100, 33098 Paderborn, Germany*
(Received 6 August 2009; revised manuscript received 20 October 2009; published 20 November 2009)

The effects of hydrogenation on Mn-doped GaN are studied with electron-paramagnetic resonance (EPR), local vibrational mode (LVM) spectroscopy, and density-functional theory (DFT) calculations. With EPR, we find two distinct Mn complexes which, in particular, differ in the size and orientation of the uniaxial crystal field and are attributed to Mn-H complexes oriented along the out-of-plane Ga-N bonds parallel to the *c* axis and to Mn-H complexes oriented along the "in-plane" Ga-N bond directions. DFT calculations in the local spin-density approximation taking into account the self-consistent correlation parameter *U* predict that the in-plane back-bonded configuration and the out-of-plane bond-center configuration of the Mn-H complexes have the lowest, nearly identical total energy, in good agreement with the EPR results. The hyperfine interactions with the Mn nucleus in the different complexes are fully reproduced by the theory. Using infrared-absorption and reflection measurements, we additionally observe the stretching mode of the in-plane configuration and report the effects of H/D substitution and measurement temperature on the LVM.

DOI: 10.1103/PhysRevB.80.205205 PACS number(s): 75.50.Pp, 76.30.Da, 78.30.Fs, 63.20.Pw

I. INTRODUCTION

Hydrogen is an important impurity in semiconductors since it allows tuning of the electronic, the structural, as well as the magnetic properties. It can, in particular, deactivate dopants and defects via the formation of hydrogen complexes, which is of major importance for the functionality of many semiconductor devices ranging from field-effect transistors to thin-film solar cells.[1,2] However, the detailed microscopic structure of these complexes often is subject to ongoing debate. Typically, their characteristic local vibrational modes (LVMs) are compared with expectations from *ab initio* calculations to obtain an understanding of the microscopic structure.

Electron paramagnetic resonance (EPR) is also a powerful technique to elucidate the microscopic structure of paramagnetic defects or defect complexes. However, only a few selected defect-hydrogen complexes, the Pt-H_2 complex in Si,[3,4] gold-hydrogen complexes in Si,[5] or the nitrogen-vacancy-hydrogen complex in diamond[6] could be studied by EPR until now. The high spin state of Mn in its 2+ oxidation state with an electron spin $S=5/2$ and a nuclear spin $I=5/2$ lends itself in a near perfect way to study both the crystal-field anisotropies induced by the formation of Mn-H complexes as well as the electron polarization reflected in the hyperfine interaction. Mn-H complexes with Mn in the 2+ oxidation state are formed in III-V semiconductors upon hydrogenation.[7–10] The passivation of the acceptor properties of substitutional Mn on the group III lattice site by complex formation leads to a reversible suppression of the hole-mediated ferromagnetism in $Ga_{1-x}Mn_xAs$ and $Ga_{1-x}Mn_xP$ with $0.02 \lesssim x \lesssim 0.07$.[11–13] While characteristic hydrogen LVMs of Mn-H complexes have been observed in both materials,[8–10] only broad unresolved EPR lines have been reported to date in these materials, possibly due to the high Mn concentration present in these samples needed to achieve ferromagnetic ordering in the nonhydrogenated cases.[14]

Here, we use Mn-doped GaN with significantly lower Mn concentrations in the range of 10^{20} cm^{-3}, where the interaction between neighboring Mn acceptors and therefore also Mn-H complexes is low, to study Mn-H complex formation. Indeed, in these samples we find well-resolved EPR lines of Mn-H complexes which allows to determine the microstructure of these complexes. The pronounced hydrogen-induced uniaxial crystal fields observed indicate the presence of both, in-plane (ip) antibonding and out-of-plane bond-centered complex configurations in our samples. The results are substantiated by *ab initio* calculations in the framework of density-functional theory (DFT) whereby correlation effects beyond the usual local spin-density approximation (LSDA) are taken into account in an LSDA+*U* approach. The calculated data presented here confirm not only the energetic preference of the two complex configurations but also the hyperfine splittings observed in the EPR measurements are reproduced. To complete the structural analysis based on EPR data, we are also able to observe the stretching LVM at 3101 cm^{-1} of the in-plane antibonding Mn-H complex.

II. EXPERIMENTAL DETAILS

Several manganese doped as well as Mn and Si codoped samples discussed in detail in Ref. 15 were used for the present study. They were grown by plasma-induced molecular-beam epitaxy on [0001]-oriented sapphire substrates and have a thickness of about 1.2 μm. As described below, the detailed analysis will focus on a particular GaN:Mn sample grown at a temperature of about 815 °C. A comparison of the total Mn concentration $[Mn^{tot}] \approx 1 \times 10^{20}$ cm^{-3} derived from elastic recoil detection with the concentration of Mn in the 2+ charge state $[Mn^{2+}] \approx 2 \times 10^{18}$ cm^{-3} as deduced from EPR demonstrated that in the as-grown sample Mn is predominantly in the 3+ charge state,

in agreement with superconducting quantum interference device magnetometry and optical-absorption measurements.[15]

Hydrogenation was carried out in a remote dc hydrogen plasma system operated at 0.7 mbar for 2 h with the sample heated to 600 °C, characteristic for acceptor passivation in GaN.[16] For the identification of the local vibrational modes, some GaN:Mn samples were deuterated in the plasma system.

The EPR measurements were performed with a Bruker ESP 300 electron-paramagnetic resonance spectrometer with a TE_{102} cavity at a constant microwave frequency $\omega/2\pi \approx 9.3$ GHz with the sample temperature adjusted to 5 K using a liquid-He flow cryostat. For lock-in detection we apply magnetic field modulation with amplitude $\mu_0 H_{\mathrm{mod}}=1.8$ mT and frequency $f_{\mathrm{mod}}=100$ kHz.

Local vibrational-mode spectroscopy was performed with a Fourier-transform infrared (FTIR) spectrometer (Bruker VERTEX 70v). Room-temperature infrared absorption was measured by attenuated total reflection (ATR) at an instrumental resolution of 1.5 cm^{-1} with a deuterated L-alanine doped triglycene sulfate detector. Furthermore, we performed comparative infrared transmission measurements at room temperature and at 8 K using a mercury cadmium telluride detector.

III. CHANGE IN THE EPR PATTERN UPON HYDROGENATION

The parameters of the spin Hamiltonian for isolated $^{55}Mn^{2+}$ centers with electronic spin $S=5/2$ and nuclear spin $I=5/2$ in GaN have already been determined in detail[17] from the angular dependence of EPR of partially compensated samples with $[Mn^{2+}] \approx 3\times 10^{19}$ cm^{-3}. Compensation is either provided by shallow-impurity donors or intentional Si codoping. For samples which already exhibit such a quite high Mn^{2+} concentration ($0.1 \leq [Mn^{2+}]/[Mn^{tot}] \leq 1$), we did not observe a change in the EPR pattern upon hydrogenation. However, $Ga_{1-x}Mn_xN$ samples with similar $[Mn^{tot}] \approx 1\times 10^{20}$ cm^{-3} but a lower degree of compensation and thus a lower concentration $[Mn^{2+}] \approx 2\times 10^{18}$ cm^{-3}, exhibited a significant change in their EPR pattern upon hydrogenation (cf. Fig. 1). This change consists both of an increase in EPR signal intensity of the central fine-structure resonance line group by a factor of 5 and the appearance of additional fine-structure resonance line groups at 235 mT $< \mu_0 H <$ 275 mT and 375 mT $< \mu_0 H <$ 415 mT for magnetic field directions $\vec{H} \| [\bar{1}2\bar{1}0]$, exhibiting an angular dependence different from the one observed for isolated $^{55}Mn^{2+}$ centers in compensated GaN samples before.[17] These changes can be reversed almost completely upon subsequent annealing in vacuum for 2 h also at 600 °C (cf. Fig. 1).

A. Anisotropy of the EPR pattern within the (0001) epitaxial layer plane

To investigate the angular dependence of the EPR pattern after hydrogenation we performed EPR measurements for the external magnetic field rotated in the $(10\bar{1}0)$ as well as within the (0001) layer plane. For the rotation of the external magnetic field within the film plane, the isolated $^{55}Mn^{2+}$ centers in compensated GaN samples do not exhibit an anisotropy in agreement with their known symmetry.[17] In contrast, upon hydrogenation we observe a clear 60° periodicity of fine-structure resonance line groups at 235 mT $< \mu_0 H <$ 275 mT and 375 mT $< \mu_0 H <$ 415 mT [cf. Fig. 2(a)]. In the false color rendering of the EPR spectra of the in-plane rotation of the external magnetic field depicted in Fig. 2(b), even additional fine-structure resonance line groups at 180 mT $< \mu_0 H <$ 220 mT and 450 mT $< \mu_0 H <$ 490 mT with the same periodicity can be distinguished. Note that since the EPR signal represents the derivative of the microwave absorption the position of a resonance in this representation is given by values of the external magnetic field where the EPR signal intensity decreases rapidly, i.e., where the color changes rapidly in Fig. 2(b). The additional fine-structure line groups are resolved also with a periodicity of 60°, i.e., whenever the external magnetic field is aligned along a $\langle \bar{1}2\bar{1}0 \rangle$ axis. These directions correspond to the in-plane orientations perpendicular to the Ga-N bond directions which are tilted by ≈19.5° with respect to the (0001) film plane. Viewed from the possible Ga lattice sites of a Mn atom there are six different "in-plane" Mn-N bond directions which in the top-view representation in Fig. 2(d) are projected along the $\langle 10\bar{1}0 \rangle$ axes. Note that we use the notation in plane although the Mn-N bond axes are not oriented exactly within the film plane. Furthermore, we emphasize that the top view in Fig. 2(d) does not represent a top view of the GaN crystal shown in Fig. 2(c) but illustrates all in-plane Mn-N bond axis orientations with respect to Mn atoms on Ga lattice sites, taking into account the fact that there are two

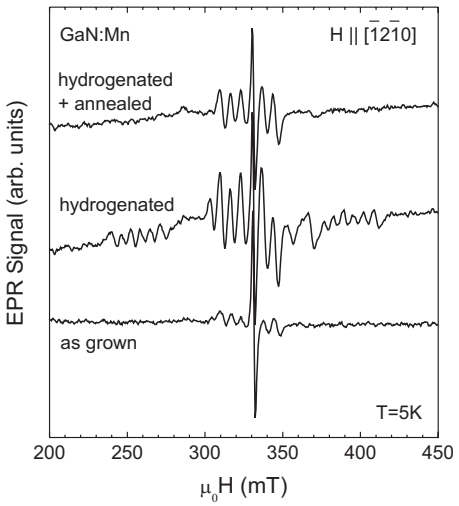

FIG. 1. *X*-band EPR spectra of $Ga_{1-x}Mn_xN$ with the external magnetic field oriented parallel to $[\bar{1}2\bar{1}0]$ at 5 K. Hydrogenation leads both to an increase in EPR signal intensity of the central fine-structure resonance line group at 310 mT $< \mu_0 H <$ 350 mT by a factor of 5 and the appearance of additional fine-structure resonance line groups at 235 mT $< \mu_0 H <$ 275 mT and 375 mT $< \mu_0 H <$ 415 mT exhibiting an angular dependence different to the one observed for isolated $^{55}Mn^{2+}$ centers in compensated GaN samples before (Ref. 17). The changes can be reversed almost completely upon subsequent annealing for 2 h at 600 °C.

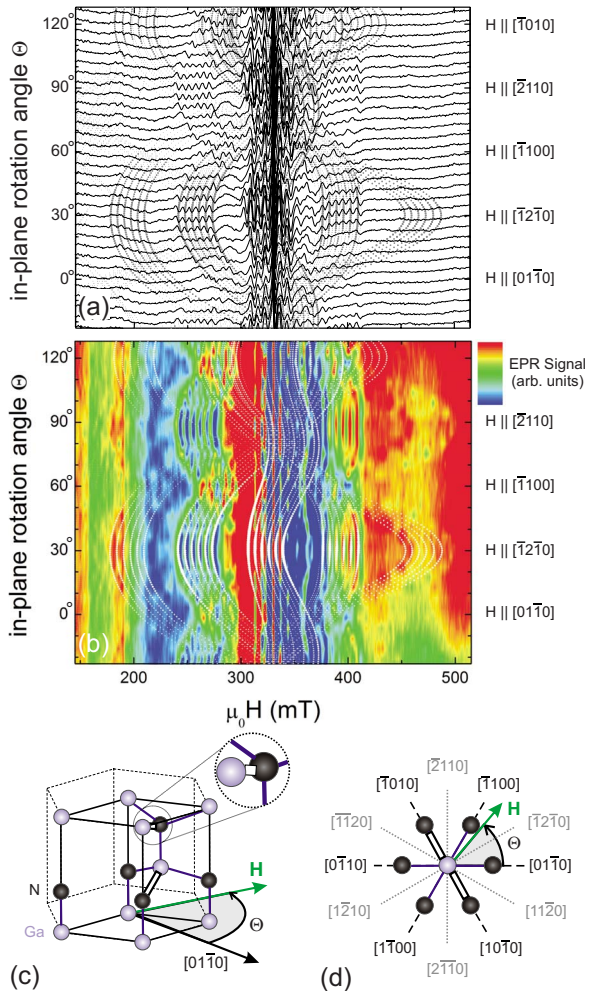

FIG. 2. (Color online) (a) Original data and (b) false color rendering of the EPR signal intensity of $Ga_{1-x}Mn_xN$ after hydrogenation for a rotation of the external magnetic field within the film plane (0001) at 5 K. The circles represent the result of a simulation taking into account a uniaxial crystal-field anisotropy D_H^{ip}=−46.5 mT $g\mu_B$ due to Mn-H complex formation along one of the Ga-N bond axes plotted via a thick white line in the three-dimensional (3D) representation (c) of the GaN crystal structure. With respect to Mn atoms at Ga lattice sites the Mn-N bond axes can be oriented along seven different crystallographic orientations, $[01\bar{1}\frac{1}{8}]$, $[\bar{1}10\frac{1}{8}]$, $[\bar{1}01\frac{1}{8}]$, $[0\bar{1}1\frac{1}{8}]$, $[1\bar{1}0\frac{1}{8}]$, $[10\bar{1}\frac{1}{8}]$, and [0001]. Figure (d) illustrates the six in-plane orientations in top view. Mn-H complex formation along one of the two bond axes plotted via a thick white line accounts for the uniaxial crystal-field anisotropy D_H^{ip} used for the simulation in (a) and (b). Note that the top view in (d) does not represent a top view of the GaN crystal in (c) but illustrates all possible Mn-N bond axis orientations with respect to Mn atoms on the two inequivalent Ga sites.

nonequivalent Ga lattice sites per unit cell in the GaN host lattice where the Mn atom could be incorporated.

B. Simulation of the EPR pattern within the epitaxial layer plane

We have performed a simulation of the in-plane EPR pattern [cf. Figs. 2(a) and 2(b)] employing the spin Hamiltonian

$$\mathcal{H}_S = g\mu_B\mu_0\vec{H}\vec{S} + A\vec{S}\vec{I} + \vec{S}\hat{D}_{[0001]}\vec{S} + \vec{S}\hat{D}_H\vec{S}, \qquad (1)$$

taking into account the Zeeman interaction with the g factor g^{ip}=2.014 and an isotropic hyperfine interaction with the hyperfine constant A^{ip}=−6.6 mT $g\mu_B$ discussed in more detail below (with the conversion factor 1 mT $g\mu_B$=116 neV). $\vec{S}$ and $\vec{I}$ are the electronic and nuclear-spin operators, respectively. To allow an explicit discussion of the influence of the H atom, the fine structure of the levels in the zero-field limit is parametrized by two uniaxial crystal-field anisotropies in growth direction (along the hexagonal crystal axis) and along an ip Ga-N bond direction parametrized by the matrices $\hat{D}_{[0001]}$ and $\hat{D}_H=\hat{D}_H^{ip}$, respectively. For the axial symmetric contribution in growth direction ($\hat{D}_{[0001],ij}=0$ for $i\neq j$) we used $\hat{D}_{[0001],xx}=\hat{D}_{[0001],yy}=-D_{[0001]}/3$ and $\hat{D}_{[0001],zz}=2D_{[0001]}/3$ with the value $D_{[0001]}$=−23.6 mT $g\mu_B$ taken from the spectrum of the isolated Mn^{2+} ion. Within a superposition model for the spin-orbit coupling[17,18] this particular value can be explained by a displacement $\delta_{[0001]}$=0.085 Å of the Mn^{2+} atoms from the exact Ga^{3+} site toward the N ligand along growth direction as discussed in Ref. 17.

The crystal-field anisotropy $\hat{D}_H$ is introduced to account for the additional reduction in symmetry due to the formation of Mn-H complexes. In a simple model the H atom is incorporated either in a bond-centered position between the Mn and a neighboring N atom, or in a position back bonded to a neighboring N atom. Both configurations would induce an additional uniaxial crystal-field anisotropy, described by a matrix $\hat{D}_H$, which is obtained from the appropriate rotation of the principal axis of $\hat{D}_{[0001]}$ into the direction of the corresponding Mn-N bond axis.

The simulation resulting in the angular dependence of resonance fields represented by the gray (white) circles in Figs. 2(a) and 2(b) was performed for a uniaxial crystal-field anisotropy D_H^{ip}=−46.5 mT $g\mu_B$ along one of the Mn-N bond axes marked via thick white lines in Figs. 2(c) and 2(d) (i.e., along $[10\bar{1}\frac{1}{8}]$ or $[\bar{1}01\frac{1}{8}]$), which both result in the same in-plane angular dependence of the resonance fields. As for all simulations presented in the following, the theoretical intensity of the transitions is coded by the diameter of the dots.[17] This crystal-field contribution well describes the positions and angular dependences of the additional fine-structure line groups upon hydrogenation for $0°<\Theta<60°$. Furthermore, the 60° periodicity of the EPR pattern straightforwardly follows from the contribution of Mn-H complexes along the remaining in-plane Mn-N bond axes (i.e., along $[01\bar{1}\frac{1}{8}]$, $[\bar{1}10\frac{1}{8}]$, $[0\bar{1}1\frac{1}{8}]$, and $[1\bar{1}0\frac{1}{8}]$).

C. EPR pattern in the (10$\bar{1}$0) plane

The EPR pattern for the rotation of the external magnetic field in the (10$\bar{1}$0) plane [cf. Figs. 3(a) and 3(d)] can be analyzed in the same way. The gray circles in Fig. 3(a) show the result of a simulation for complex formation along $[\bar{1}01\frac{1}{8}]$ with the same set of parameters g^{ip}=2.014, A^{ip}=−6.6 mT $g\mu_B$, $D_{[0001]}$=−23.6 mT $g\mu_B$, and D_H^{ip}=

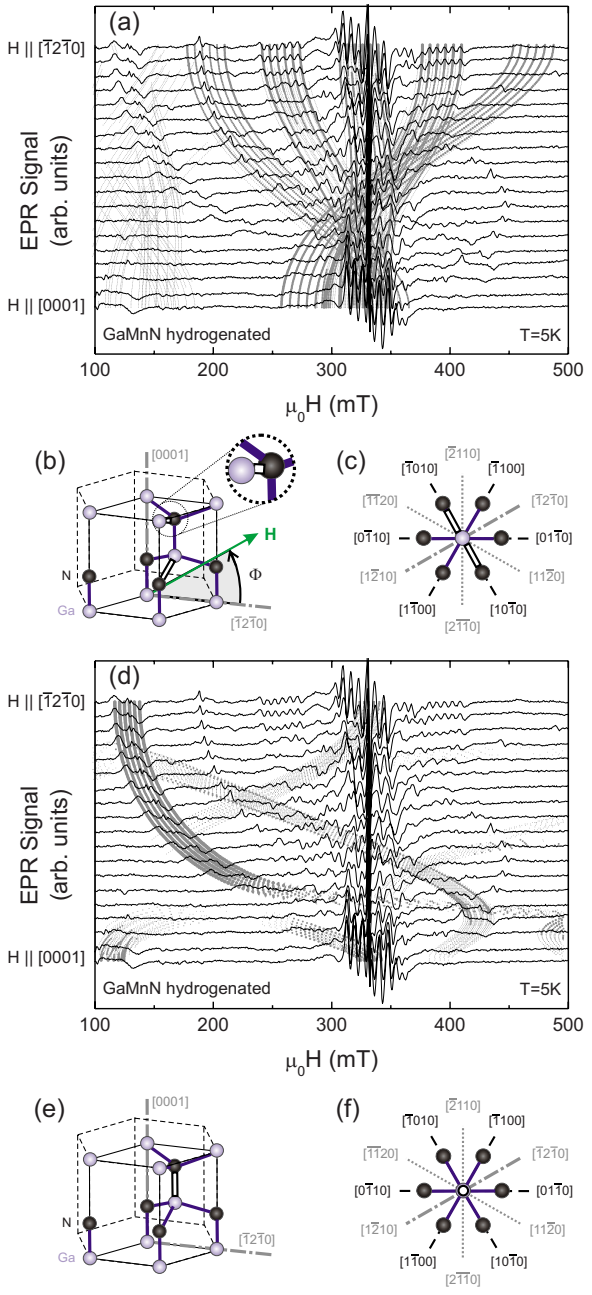

FIG. 3. (Color online) Angular dependence of the EPR at 5 K of $Ga_{1-x}Mn_xN$ upon hydrogenation for the external magnetic field rotated in 5° steps within the $(10\bar{1}0)$ plane. The gray circles in (a) represent the result of a simulation with $g^{ip}=2.014$, $A^{ip}=-6.6$ mT $g\mu_B$, $D_{[0001]}=-23.6$ mT $g\mu_B$, $D_H^{ip}=-46.5$ mT $g\mu_B$, and the principal axis of the $\hat{D}_H$ tensor rotated into the direction of the $[\bar{1}01\frac{1}{8}]$ Mn-N bond axis. Due to symmetry reasons a rotation into the $[10\bar{1}\frac{1}{8}]$ axis yields the same result. The gray circles in (d) represent the result of a simulation with $g^{op}=1.984$, $A^{op}=-4.2$ mT $g\mu_B$, and $D_H^{op}=-223.5$ mT $g\mu_B$. Again, the $[01\bar{1}\frac{1}{8}]$, $[\bar{1}10\frac{1}{8}]$, and [0001] axes are represented by thick white lines in the 3D representation of the GaN crystal structure in (b) and (e) as well as in the top views (c) and (f) illustrating all possible in-plane Mn-N bond axes orientations with respect to the Mn atoms on the two inequivalent Ga lattice sites and the out-of-plane Mn-N bond axis, respectively.

−46.5 mT $g\mu_B$ already used for the description of the in-plane angular dependence of EPR in Fig. 2. This simulation accounts for the positions and the angular dependencies of the fine-structure resonance groups experimentally observed at 235 mT$<\mu_0H<$275 mT and at 375 mT$<\mu_0H<$415 mT for $\vec{H}\|[\bar{1}2\bar{1}0]$ and the double-resonance structure at 355 mT$<\mu_0H<$365 mT for $\vec{H}\|[0001]$ [cf. Fig. 3(a)]. Note, however, that the central part of the out-of-plane EPR pattern is dominated by the overlap of the contributions from complex formation along the different Mn-N bond axes, which hampers the identification of the individual anisotropies.

So far we have only taken into account complex formation along the in-plane Mn-N bond axes. However, we also observe complex formation along the Mn-N bond axis in growth direction [cf. Figs. 3(e) and 3(f)]. We simulate the EPR patterns of this complex again using Eq. (1) with an "out-of-plane" (op) g factor $g^{op}=1.984$ and an isotropic $A^{op}=-4.2$ mT $g\mu_B$. For a useful simulation, a single axially symmetric crystal field in [0001] direction is required, which for reasons of notation symmetry we denote $\hat{D}_H^{op}$ rather than $\hat{D}_{[0001]}$. Using a value of $D_H^{op}=-223.5$ mT $g\mu_B$, we obtain the angular dependence of the EPR pattern illustrated by the gray circles in Fig. 3(d). In particular, this simulation accounts for the EPR signal at 110 mT$<\mu_0H<$145 mT for $\vec{H}\|[\bar{1}2\bar{1}0]$ as well as its angular dependence, the EPR signal at 410 mT$<\mu_0H<$440 mT observed for $\vec{H}$ rotated about 15° with respect to [0001], and the EPR signal at 110 mT $<\mu_0H<$145 mT for $\vec{H}\|[0001]$. Note that the value for $D_H^{op}=-223.5$ mT $g\mu_B$ is about one order of magnitude larger than $D_{[0001]}=-23.6$ mT $g\mu_B$ typically observed for partially compensated as-grown $Ga_{1-x}Mn_xN$ samples. Furthermore, D_H^{op} is about a factor of five larger than $D_H^{ip}=-46.5$ mT $g\mu_B$ derived for in-plane Mn-H complexes. This huge difference in the uniaxial crystal-field anisotropy induced by Mn-H complex formation "within" the film plane and along growth direction strongly indicates a different Mn-H structure for both orientations. Since the magnitude of the uniaxial crystal-field anisotropy depends on the extent of the lowering of the local symmetry, the smaller D_H observed for the in-plane complexes suggests a Mn-H complex configuration with the hydrogen atom incorporated more distant from the Mn atom as, e.g., would be the case for the antibonding configuration. In contrast, the much larger uniaxial crystal-field anisotropy for Mn-H complex formation along growth direction indicates a configuration where the H atom strongly distorts the lattice in the vicinity of the Mn atom, as would be the case for the bond-centered configuration. We will substantiate these conclusions by means of DFT calculations below.

Note that the negative signs of $D_{[0001]}$ and A of the as-grown samples are based on the analysis of the temperature dependence of the EPR signal intensities of the different fine-structure resonance line groups in Ref. 17. Using also a negative $D_{[0001]}$ for the hydrogenated samples, our simulations are able to account for the anisotropy of the in-plane Mn-H complexes only for a negative D_H^{ip}. The anisotropy observed in the EPR pattern of the out-of-plane Mn-H com-

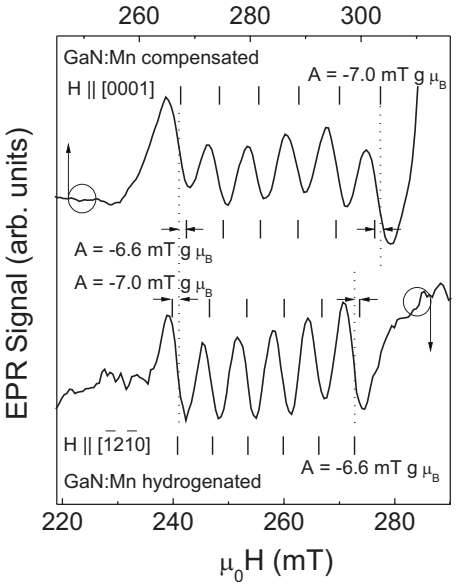

FIG. 4. Comparison of hyperfine splittings of a compensated and a hydrogenated $Ga_{1-x}Mn_xN$ sample. The vertical lines above and below each spectrum represent simulated resonance positions for hyperfine interaction parameters $A=-7.0$ mT $g\mu_B$ and $A=-6.6$ mT $g\mu_B$, respectively. The other parameters used in the corresponding spin Hamiltonian are $g^{\mathrm{comp}}=1.994$ and $D^{\mathrm{comp}}_{[0001]}=-22.4$ mT $g\mu_B$ for the compensated sample and $g^{\mathrm{ip}}=2.014$, $D_{[0001]}=-23.6$ mT $g\mu_B$, and $D^{\mathrm{ip}}_{\mathrm{H}}=-46.5$ mT $g\mu_B$ for the hydrogenated sample. As indicated by the small arrows, the hyperfine splitting of the resonances of the compensated sample is best reproduced by $A^{\mathrm{comp}}=-7.0$ mT $g\mu_B$ while the hydrogenated sample exhibits a slightly smaller $A^{\mathrm{ip}}=-6.6$ mT $g\mu_B$. Note that due to the additional crystal-field anisotropy described by $D^{\mathrm{ip}}_{\mathrm{H}}$ the fine-structure resonance line groups are well resolved at different orientations of the external magnetic field. Although only isotropic hyperfine interactions are taken into account, the fine-structure terms in the Hamiltonian (1) lead to the anisotropy of the hyperfine splitting observed in experiment which is fully reproduced by the simulation.

plexes could, in principal, also be explained by a positive $D^{\mathrm{op}}_{\mathrm{H}}$ of similar magnitude, however the negative sign is inline with the superposition model discussed in Ref. 17.

Finally, we want to point out that the resonance at 110 mT$<\mu_0 H<$145 mT for $\vec{H}\|[\bar{1}2\bar{1}0]$ exhibits vanishing intensity if the sample is mounted for the in-plane rotation. This finding is reproduced by our simulation and can be explained by a suppression of the corresponding transition rate resulting from Fermi's golden rule when the microwave magnetic field $\vec{h}_{\mathrm{rf}}$ is oriented along the growth direction. For a rotation of the external magnetic field within a specific crystallographic plane, the microwave magnetic field $\vec{h}_{\mathrm{rf}}$ is oriented perpendicularly to this plane, i.e., along the axis of rotation. Thus for the in-plane rotation $\vec{h}_{\mathrm{rf}}$ is oriented along the growth direction while for the rotation of the external magnetic field in the $(10\bar{1}0)$ plane $\vec{h}_{\mathrm{rf}}$ is aligned along $[10\bar{1}0]$.

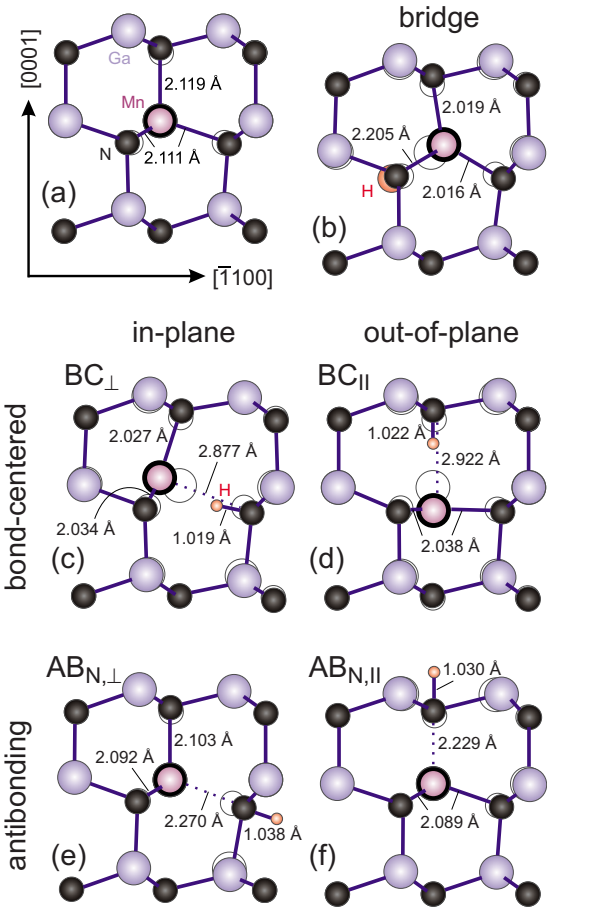

FIG. 5. (Color online) Schematic representation of the atomic positions projected into the $(11\bar{2}0)$ plane as derived from LSDA $+U_{\mathrm{sc}}$ DFT calculations for (a) Mn^{2+} and Mn-H complexes in the (b) in-plane bridge, (c) in-plane bond-centered ($BC_{\perp}$), (d) out-of-plane bond-centered ($BC_{\|}$), (e) in-plane antibonding ($AB_{N,\perp}$), and (f) out-of-plane antibonding ($AB_{N,\|}$) configurations in wurtzite GaN. In the bridge configuration the hydrogen atom is incorporated in between two N atoms. To clarify its position it is plotted with an increased atomic radius in (b). The open circles indicate the atomic positions of the unstrained GaN lattice.

D. Change in hyperfine splitting

Besides the change in the fine-structure splitting, we also find a change in the hyperfine splitting upon hydrogenation. As shown in Fig. 4, the fine-structure line group related to the in-plane Mn-H complexes exhibits a slightly smaller hyperfine splitting parameter $A^{\mathrm{ip}}=-6.6$ mT $g\mu_B$ compared to $A^{\mathrm{comp}}=-7.0$ mT $g\mu_B$ typically observed for a compensated sample. For the Mn-H complexes along the [0001] growth direction, the hyperfine splitting is not resolved. However, we still are able to derive a value for A^{op} from the peak-to-peak line widths of the related fine-structure line groups. As shown in Fig. 3(d) the widths of the whole fine-structure line groups at 110 mT$<\mu_0 H<$145 mT for $\vec{H}\|[\bar{1}2\bar{1}0]$ and at 410 mT$<\mu_0 H<$440 mT observed for $\vec{H}$ rotated by about 15° with respect to [0001] are well reproduced by the result of the simulation for Mn-H complex formation along growth direction with $A^{\mathrm{op}}\approx-4.2$ mT $g\mu_B$, which is significantly

TABLE I. Parameters used in Eq. (1) for the simulation of the angular dependence of the EPR spectra in Figs. 2–4. The biaxial compressive strain of the as-grown samples is given by ϵ_a. Here, "Mn^{2+}, ϵ_a=−0.04%" refers to the virtually unstrained as-grown $Ga_{1-x}Mn_xN$ sample exhibiting a low degree of compensation studied in detail that shows the additional fine-structure line groups upon hydrogenation while "Mn^{2+}, ϵ_a=−0.18%" refers to a highly compensated as-grown sample that does not show a change in the EPR pattern upon hydrogenation. "Mn^{2+}-H^{ip}" and "Mn^{2+}-H^{op}" denote the Mn-H complexes within the film plane and along the growth direction, respectively.

Configuration	ϵ_a (%)	g	$A(^{55}Mn)$ (mT $g\mu_B$)	$D_{[0001]}$ (mT $g\mu_B$)	D_H^{ip} (mT $g\mu_B$)
Mn^{2+}	−0.04	1.989	−7.0	−23.6	
	−0.18	1.994	−7.0	−22.4	
Mn^{2+}-H^{ip}		2.014	−6.6	−23.6	−46.5
Mn^{2+}-H^{op}		1.984	−4.2	D_H^{op}=−223.5	

smaller than A^{ip}=−6.6 mT $g\mu_B$ observed for the in-plane complexes. Table I summarizes the parameters of the spin Hamiltonian (1) derived from these experiments.

IV. COMPARISON WITH THE RESULTS OF DFT CALCULATIONS

A. Method

To further analyze the Mn-H microstructure in hexagonal GaN we performed comparative total-energy calculations in the framework of DFT using the gradient-corrected Perdew-Burke-Ernzerhof functional[19] taking into account correlation effects of the strongly localized Mn 3*d* electrons within a spin-polarized LSDA+*U* approach. We use 96 atom supercells, norm-conserving pseudopotentials, and a 2×2×2 Monkhorst-Pack *k*-point set[20] to determine the possible atomic configurations of the Mn-H microstructure. Furthermore, the hyperfine splittings of the most stable paramagnetic defect structures with total spin $S=5/2$ are calculated taking into account relativistic effects in scalar-relativistic approximation[21,22] as recently implemented in the gauge-including projector augmented plane-wave extension[23] of the QUANTUM ESPRESSO package.[24]

Taking advantage of the nonlinear core correction,[25] a plane-wave basis set is used with an energy cutoff of 70 Ry treating the Ga 3*d* electrons in the frozen core. For intrinsic defect structures, this treatment was shown to provide within 1% the same hyperfine splitting as the computationally much more demanding treatment within the valence.[26] The efficient treatment of the 3*d* electrons of the Ga host atoms allows us to take into account correlation effects of the strongly localized Mn 3*d* electrons within a spin-polarized LSDA+U_{sc} approach whereby the correlation parameter U_{sc} is determined self-consistently as described in Ref. 27.

B. Results of the total-energy calculations

LSDA+U_{sc} total-energy calculations are performed for a set of plausible Mn-H complex configurations in wurtzite GaN and are summarized in Fig. 5 and Table II. However, we first investigate the isolated Mn^{2+} ion as a basic reference system. As illustrated in Fig. 5(a), we obtain a rather minor reduction in symmetry characterized by a distance to the N ligand in growth direction (2.119 Å), which is 0.008 Å larger than the distances to the N ligands within the film plane (2.111 Å). Hence, the earlier assertion of a displacement from the substitutional Ga site toward the N ligand in growth direction by $\delta_{[0001]}$=0.085 Å (cf. Ref. 17) could not be corroborated, suggesting that the simple superposition model[18] for the spin-orbit coupling presented in Ref. 17 has to be applied with care at least for structures with small displacements. For Mn-H complexes however, rather large displacements are expected so that an application of the superposition model[18] seems to be more reasonable. We will come back to this point later in Sec. IV D.

Because of the hexagonality of the wurtzite crystal we have to take into account bond-centered and antibonding incorporation of the H atom with respect to a Mn-N bond in in-plane as well as in out-of-plane configuration. In both cases the antibonding configuration leads to only minor lattice distortions. The H atom binds to one of the N ligands that, as a consequence, moves away from the Mn^{2+} ion whereby the Mn^{2+} ion itself remains more or less at the regular lattice site as in the case of the isolated Mn^{2+} ion. The bond-centered configuration, in contrast, leads to a strong relaxation of the Mn atom into the plane defined by the three distant N ligands [see e.g., Fig. 5(d)]. According to our LSDA+U_{sc} calculations, the in-plane antibonding ($AB_{N,\perp}$)

TABLE II. Calculated formation energies of the Mn-H complex configurations with respect to the H^+ ion at the interstitial site (in between four N neighbors). The results are given both for LSDA and LSDA+U_{sc}. The self-consistently determined values U_{sc} are also given. Note that for the isolated Mn ion a value U_{sc} =4.67 eV was obtained.

Configuration	LSDA (eV)	U_{sc} (eV)	LSDA+U_{sc} (eV)
Bridge	−0.053	4.42	+0.047
$AB_{N,\parallel}$	−0.714	4.77	−0.751
$BC_{\perp}$	−0.942	4.29	−0.903
$BC_{\parallel}$	−1.111	4.27	−1.031
$AB_{N,\perp}$	−1.003	4.75	−1.050

configuration depicted in Fig. 5(e) is energetically most favorable. However, the out-of-plane bond-centered ($BC_{\parallel}$) configuration in Fig. 5(d) is only 19 meV higher in energy. The in-plane bond-centered ($BC_{\perp}$) configuration in Fig. 5(c) and the out-of-plane antibonding ($AB_{N,\parallel}$) configuration in Fig. 5(f) are higher in energy by 147 and 299 meV, respectively. Note that almost identical atomic positions are obtained already by plain LSDA. However, the relative stability of the different Mn-H complexes is affected considerably by the LSDA+U_{sc} approach (cf. Table II): in LSDA the $BC_{\parallel}$ configuration is favored by 0.11 eV in comparison to the $AB_{N,\perp}$ configuration. The latter becomes the ground state only if the correlation effects are explicitly taken into account within the LSDA+U_{sc} approach. In this approach the formation energy of the antibonding configurations is decreased by about 0.05 eV with respect to the plain LSDA values whereas the formation energy of all other complexes is increased by roughly 0.1 eV. Note that this is not simply a consequence of the larger U_{sc} values for the antibonding configurations of about 4.8 eV instead of 4.3 eV in case of the bond-centered configurations since a larger U_{sc} even increases the energies of the antibonding configurations. With a common U_0 =4.5 eV for all configurations the relative stability of the antibonding configurations would be increased by 0.25 eV compared to the LSDA values, about twice the difference obtained when using the self-consistently determined correlation parameter U_{sc}. However, in comparison with the usual LSDA, the explicit treatment of electron correlation in the open 3*d* shell of the Mn atom makes the $AB_{N,\perp}$ configuration slightly more stable than the axial counterpart where the H atom is incorporated at the bond-centered position. Most importantly, LSDA+U_{sc} predicts that the two competing structures are very similar in total energy.

The $AB_{N,\perp}$ configuration of an Mg-H complex has already been identified as the energetically most favorable one in Mg-doped GaN at 0 K.[28,29] However, at elevated temperatures a different configuration denoted out-of-plane off-axis ($OA_{\parallel}$) has been reported to become more stable driven by entropy.[28,29] This would account for the angle of $130 \pm 5°$ between the N-H bond and the [0001] axis derived experimentally via multitransmission infrared spectroscopy with polarized light by Clerjaud *et al.*[30] In analogy we also took the $OA_{\parallel}$ configuration as a starting structure for the total-energy calculations of the Mn-H complex. However, we found that without any energy barrier the H atom relaxes back into the energetically more favorable $BC_{\parallel}$ configuration. Note that this behavior, the absence of a local minimum for an off-axis configuration, is independent of the value of the correlation parameter U_{sc}. Instead, we found an additional local minimum, where the hydrogen atom is positioned in between two N ligands within the film plane [see also Fig. 5(b)]. However, this bridge configuration comes out to be about 1 eV higher in energy than the most favorable structures.

C. Comparison with the experimental results for the hyperfine splitting

The isotropic part of the hyperfine (hf) splitting of the central Mn ion is predominantly caused by Fermi-contact interaction of the spin polarization of the *s* orbitals induced by the 3*d* electrons at the ^{55}Mn nucleus. For comparison, the hyperfine splitting of the free Mn^{2+} ion due to the polarization of the 1*s*, 2*s*, and 3*s* shells by the half-filled 3*d* shell is expected to be −10.9 mT $g\mu_B$.[31] If the Mn ion is incorporated in a host material the absolute value of hf splitting can be considerably reduced, by hybridization and lattice distortion.[32] The values −7.0 mT $g\mu_B$, −6.6 mT $g\mu_B$, and −4.2 mT $g\mu_B$ perfectly fit in this simple picture if assuming an increasing lattice distortion for the Mn^{2+}, Mn^{2+}-H^{ip}, and Mn^{2+}-H^{op} centers, respectively, as already suggested by the fine-structure splittings (see also Table I).

In our DFT calculations we took into account explicitly the contributions arising from the 3*s*, 3*p*, and 3*d* valence electrons since they contribute to the interaction of the Mn ion with the surrounding and are responsible for the reduction in the hf splitting from the maximum value given by the free Mn^{2+} ion. The electrons in the 1*s* and 2*s* shells, in contrast, are treated in frozen-core approximation. They however contribute considerably to the hyperfine splittings via the so-called core polarization. For a given occupation of the Mn 3*d* shell, e.g., for all $S=5/2$ systems with $3d^5$ configuration, this contribution is expected to be independent of the hybridization.[33] Thus, we can take the isolated Mn^{2+} ion on a Ga lattice site [cf. Fig. 5(a)] as a reference system. From DFT, we calculate a valence polarization contribution to the hyperfine splitting $A^{valence}$=+7.3 mT $g\mu_B$. The deviation from the experimentally observed hyperfine splitting has to be attributed to the core-polarization contribution $A^{core}=A^{exp}-A^{valence}$=−7.0 mT $g\mu_B$−7.3 mT $g\mu_B$=−14.3 mT $g\mu_B$ of the 1*s* and 2*s* core electrons. All isotropic parts of the hyperfine splittings in Table III have been corrected by this value for the core polarization.

The isotropic parts of the hyperfine splitting $A^{iso}=(A_x+A_y+A_z)/3$ we derive in this way for the energetically most favorable Mn-H complex configurations $AB_{N,\perp}$ and $BC_{\parallel}$, namely, $A^{AB_{N,\perp}}$=−6.52 mT $g\mu_B$ and $A^{BC_{\parallel}}$=−4.09 mT $g\mu_B$, are in perfect agreement with A^{ip}=−6.6 mT $g\mu_B$ and A^{op}= −4.2 mT $g\mu_B$ observed for Mn-H complexes within the film plane and in growth direction, respectively. Since the hyperfine splitting of the central ^{55}Mn nucleus is well resolved for only some selected orientations of the external magnetic field, we were not able to compare the anisotropic part of the hyperfine tensor obtained from theory (Table III) to the EPR experiments. Table III also lists the expected splittings due to hyperfine interaction with the H^+ nucleus. However, since these values are significantly smaller than the peak-to-peak line width of an individual resonance, we were not able to resolve this splitting. Furthermore, we did not observe any difference between the anisotropic EPR pattern of hydrogenated and deuterated samples, showing that this linewidth is not dominated by unresolved hyperfine interaction with the hydrogen nuclei. According to the calculated hyperfine splittings the linewidth is mostly dominated by the hyperfine splittings due to the ^{69}Ga and ^{71}Ga nuclei at the regular Ga lattice sites instead.

D. Comparison with the experimental results for the uniaxial crystal-field anisotropies

Moreover, we can compare the uniaxial crystal-field anisotropies observed in our experiment for the Mn^{2+}-H^{op}

TABLE III. Calculated diagonal elements of the hyperfine tensor A_x, A_y, and A_z for the Mn-H complex configurations illustrated in Fig. 5, explicitly taking into account electron-correlation effects via the self-consistently determined parameter U_{sc} (see also Table II). Hyperfine splittings are given for both the Mn^{2+} nucleus as well as for the H^+ nucleus. Experimentally observed values are also given and related to the corresponding microstructures. As described in the text the isolated Mn^{2+} ion is used to estimate a correction for the core polarization. ϑ denotes the angle of the principal axis of the hyperfine tensor for a given nucleus with respect to the [0001] orientation.

Configuration		$\lvert A^{exp}\rvert$ (mT $g\mu_B$)	A_x (mT $g\mu_B$)	A_y (mT $g\mu_B$)	A_z (mT $g\mu_B$)	ϑ (deg.)
	Mn^{2+}	7.0	−7.00	−7.00	−7.00	0.0
Bridge	Mn^{2+}		−4.73	−5.05	−4.84	123.3
	H^+		−0.60	−0.63	+0.65	124.5
$AB_{N,\parallel}$	Mn^{2+}		−6.34	−6.34	−6.65	0.0
	H^+		+0.10	+0.10	+0.35	0.0
$BC_\perp$	Mn^{2+}		−2.89	−2.89	−3.60	110.1
	H^+		−0.64	−0.63	+0.74	113.7
$BC_\parallel$	Mn^{2+}	4.2	−3.90	−3.90	−4.48	0.0
	H^+		−0.65	−0.65	+0.74	0.0
$AB_{N,\perp}$	Mn^{2+}	6.6	−6.41	−6.40	−6.76	109.0
	H^+		+0.08	+0.08	+0.31	108.1

and Mn^{2+}-H^{ip} centers with the change in local symmetry as predicted by the DFT total-energy calculation. As illustrated in Fig. 5(e) for the $AB_{N,\perp}$ configuration, the distance to the accompanying N ligand is expected to increase from 2.111 to 2.270 Å by $\delta^{AB_{N,\perp}}=0.16$ Å while for complex formation in the $BC_\parallel$ configuration as shown in Fig. 5(d) we expect an increase in the associated Mn-N distance from 2.119 to 2.922 Å by $\delta^{BC_\parallel}=0.80$ Å. Indeed, the ratio of $D_H^{op}/D_H^{ip}=5$ nicely reproduces the ratio $\delta^{BC_\parallel}/\delta^{AB_{N,\perp}}=5$ suggesting that the superposition model[18] for the spin-orbit coupling gives a reasonable description for the Mn-H complexes. While the exact equality of both ratios appears to be rather coincidental, the fact that both ratios are of the same order of magnitude nevertheless again strongly indicates the presence of both the $AB_{N,\perp}$ and the $BC_\parallel$ Mn-H complex configurations in our sample.

V. CONCENTRATION OF $AB_{N,\perp}$ AND $BC_\parallel$ MN-H COMPLEXES

To determine the concentration of Mn-H complexes in the $AB_{N,\perp}$ configuration $[AB_{N,\perp}]$ we compare the intensities of the EPR fine-structure line group of the hydrogenated sample at 235 mT$<\mu_0 H<$275 mT for $\vec{H}\parallel[\bar{1}2\bar{1}0]$ in Fig. 3(a) with the intensity of the central fine-structure line group of the as-grown sample at 310 mT$<\mu_0 H<$350 mT for $\vec{H}\parallel[\bar{1}2\bar{1}0]$ (Fig. 1), taking into account the ratio of the transition intensities expected from Fermi's golden rule. Accounting also for the fact that the EPR signal of the hydrogenated sample at 235 mT$<\mu_0 H<$275 mT constitutes the superposition of the contributions of two in-plane Mn-H complexes, we obtain a concentration per in-plane Mn-H complex of $[AB^1_{N,\perp}]\approx 1\times 10^{18}$ cm^{-3}. Since there are six different in-plane Mn-H complex configurations, this adds up to a total concentration of in-plane Mn-H complexes of $[AB_{N,\perp}]=6[AB^1_{N,\perp}]\approx 6\times 10^{18}$ cm^{-3}. Applying the same analysis to the (unresolved) EPR fine-structure line group of the hydrogenated sample at 110 mT$<\mu_0 H<$145 mT for $\vec{H}\parallel[\bar{1}2\bar{1}0]$ in Fig. 3(a) we obtain a concentration of Mn-H complexes along growth direction $[BC_\parallel]\approx 1\times 10^{18}$ cm^{-3}. Taking into account that in total six in-plane and two out-of-plane Ga-N bonds are present in a primitive unit cell, the EPR concentrations determined indicate that in-plane and out-of-plane Mn-H complexes are formed approximately with the same probability. This is in agreement with the result of the DFT calculations predicting effectively the same formation energy for the $AB_{N,\perp}$ and the $BC_\parallel$ configuration.

Furthermore, the total concentration of Mn-H complexes in our sample adds up to $[\text{Mn-H}]=[AB_{N,\perp}]+[BC_\parallel]\approx 7\times 10^{18}$ cm^{-3}. For comparison, the total concentration of Mn^{2+} due to unintentional compensation in the as-grown sample amounted to $[Mn^{2+}]\approx 2\times 10^{18}$ cm^{-3} at a total Mn concentration $[Mn^{tot}]\approx 1\times 10^{20}$ cm^{-3}. Therefore, ≈10% of the Mn atoms in our sample have been passivated via Mn-H complex formation. This low-passivation efficiency might be explained by the fact that the hydrogenation temperature above which we observe a change in the EPR pattern ($T\approx 550$ °C) is close to the annealing temperature required to reverse the changes ($T\approx 600$ °C). An alternative explanation could be the vicinity of the $Mn^{3+/2+}$ charge-transfer level to the H^+/H_2 level in wurtzite GaN (Ref. 34) taking into account also the uncertainties of the calculations in Ref. 34. A position of the $Mn^{3+/2+}$ above the H^+/H_2 level would promote the formation of interstitial H_2 molecules at the expense of Mn-H complex formation but the broadening of the Fermi distribution at the hydrogenation temperature of 600 °C would still lead to a certain degree of passivation. Furthermore, also nonsubstitutional Mn would contribute to a low-passivation efficiency.

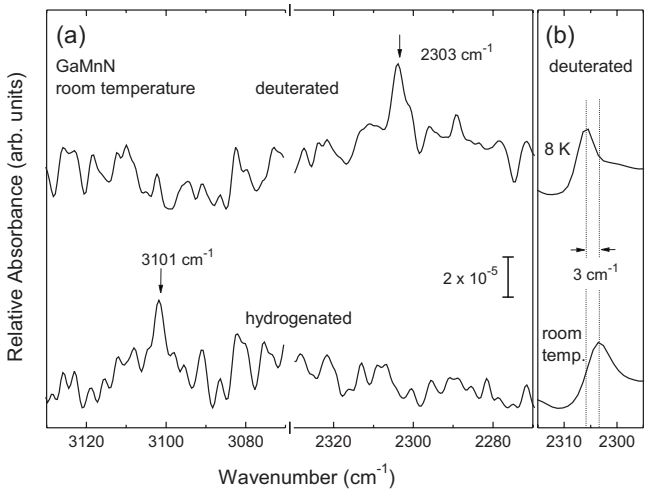

FIG. 6. (a) Room-temperature infrared-absorption spectra for $Ga_{1-x}Mn_xN$ upon hydrogenation (lower spectrum) and upon deuteration (upper spectrum). The spectra are the result of 5000 scans measured in reflectance using the ATR geometry. The arrows at 2303 and 3101 cm^{-1} mark the positions of the local vibrational modes which we attribute to the Mn-D and the Mn-H complex in the $AB_{N,\perp}$ configuration, respectively. The vertical bar indicates the magnitude of the absorbance scale. (b) Infrared absorption spectra of the deuterated sample obtained from 3000 scans measured in transmission at room temperature (lower spectrum) and at 8 K (upper spectrum).

VI. LOCAL VIBRATIONAL MODE OF THE $AB_{N,\perp}$ COMPLEX

Finally, we report the observation of the local vibrational modes of the Mn-D and the Mn-H complex in the $AB_{N,\perp}$ configuration. Figure 6(a) compares the room-temperature FTIR spectra of a hydrogenated (lower spectrum) and a deuterated $Ga_{1-x}Mn_xN$ sample (upper spectrum). The deuterated sample exhibits a mode at 2303 cm^{-1} which is shifted to 3101 cm^{-1} for the hydrogenated sample. With 1.346 the isotopic ratio of the two wave numbers which is given by the inverse ratio of the square roots of the reduced masses is close to $\sqrt{2}$ and exactly equals the ratio of the local vibrational modes of the Mg-D and the Mg-H complex at 2321 cm^{-1} and 3125 cm^{-1}, respectively, in Mg-doped GaN.[35] We consequently assign the absorption peaks at 2303 and 3101 cm^{-1} to the local vibrational modes of the Mn-D and the Mn-H complexes, respectively, in the $AB_{N,\perp}$ configuration, which is the dominant complex configuration in our samples as deduced from the EPR signal intensities above. Upon cooling to 8 K, the LVM measured in transmission geometry with the growth direction tilted by $\approx 20°$ with respect to the direction of light propagation shifts to higher wave numbers. In the case of deuterated $Ga_{1-x}Mn_xN$ shown in Fig. 6(b) the shift is 3 cm^{-1} when cooling from room temperature to 8 K. Under these polarization conditions, out-of-plane configurations such as $BC_{\parallel}$ can hardly be detected, confirming the assignment of the LVM to the H-stretching mode of the $AB_{N,\perp}$ configuration.

In Mg-doped GaN, Limpijumnong *et al.*[29] calculated the stretching modes of the Mg-H complex in the $AB_{N,\perp}$, the $OA_{\parallel}$, and the $AB_{N,\parallel}$ configuration to 3045 cm^{-1}, 3068 cm^{-1}, and 3113 cm^{-1}, respectively, but noted that the differences between these modes are smaller than the error bar of the calculations. Taking into account this uncertainty, the Mg-H mode observed by Götz *et al.*[35] at 3125 cm^{-1} is in agreement with all three complex configurations. Similarly, the vibrational mode reported here also is in agreement with these calculations. However, due to the EPR results presented here, we can assign a specific microscopic structure to the Mn-H complex giving rise to the LVM observed. Unfortunately, while via perturbed $\gamma\gamma$ angular-correlation spectroscopy[36] the existence of Cd-H complexes both within the film plane and out of plane have been reported for GaN, no LVM data, e.g., for Be, Cd, and Zn complexes are available for further comparison.

Finally we compare the signal intensity of the Mn-H localized vibration mode with the intensity expected from the optical cross section σ and the number of Mn-H complexes per area $N_{\text{Mn-H}}/A$. For the optical cross section we assume the value $\sigma \approx 10^{-19}$ cm^2 estimated for the Mg-H complexes before[35] while the number of Mn-H complexes in the $AB_{N,\perp}$ configuration per area $N_{\text{Mn-H}}/A$ can be calculated from their concentration $[AB_{N,\perp}] \approx 6 \times 10^{18}$ cm^{-3} and the film thickness $d=1.2$ μm via $N_{\text{Mn-H}}/A=[AB_{N,\perp}]d \approx 7 \times 10^{14}$ cm^{-2}. From this, we expect the absorbance $-\ln(I/I_0)=\sigma N_{\text{Mn-H}}/A \approx 7 \times 10^{-5}$, where I/I_0 denotes the reflectance with/without the sample. This value is in agreement with the absorbance $\approx 4 \times 10^{-5}$ observed in the FTIR experiment.

VII. SUMMARY

In summary, we have investigated in detail the anisotropy of the additional fine-structure line groups resulting from the hydrogenation of $Ga_{1-x}Mn_xN$. The angular dependence of the EPR pattern could be traced back to uniaxial crystal-field-anisotropy contributions in the direction of the Mn-N bond axes, where the absolute values of these contributions for the Mn-N axes oriented within the film plane $D_{\text{H}}^{\text{ip}}=-46.5$ mT $g\mu_B$ differ from the out-of-plane value $D_{\text{H}}^{\text{op}}=-223.5$ mT $g\mu_B$ by a factor of 5. We attribute this difference to Mn-H complex formation in the in-plane antibonding $AB_{N,\perp}$ and the out-of-plane bond-centered $BC_{\parallel}$ configuration, respectively. DFT calculations in LSDA+U_{sc} do not only confirm the energetic preference of both configurations but also quantitatively explain the hyperfine splittings $A^{\text{ip}}=-6.6$ mT $g\mu_B$ and $A^{\text{op}}=-4.2$ mT $g\mu_B$ derived from experiment. Furthermore, the extension of the associated Mn-N distance upon the incorporation of hydrogen by $\delta^{AB_{N,\perp}}=0.16$ Å and $\delta^{BC_{\parallel}}=0.80$ Å as derived from the DFT calculations, respectively, qualitatively accounts for the difference between D_{H}^{ip} and D_{H}^{op}. Therefore, the comparison of our experimental findings with the results of the DFT calculation demonstrates the presence of both $AB_{N,\perp}$ and $BC_{\parallel}$ Mn-H complexes in GaN:Mn+H. Our results provide information on the symmetry and structure of Mn-H complexes in GaN complementary to that usually obtained by local vibrational-mode spectroscopy.

ACKNOWLEDGMENTS

The work at the Walter Schottky Institut was supported by Deutsche Forschungsgemeinschaft under Grant No. SFB 631. W.G.S. and U.G. gratefully acknowledge financial support by DFG (Grants No. SCHM 13621/11 and No. GE 1260/3-1) as well as by CNRS.

*christoph.bihler@wsi.tum.de

[1] J. I. Pankove and N. M. Johnson, *Hydrogen in Semiconductors*, Semiconductors and Semimetals Vol. 34 (Academic, Boston, 1991).
[2] C. G. Van de Walle and J. Neugebauer, Nature (London) **423**, 626 (2003).
[3] P. M. Williams, G. D. Watkins, S. Uftring, and M. Stavola, Phys. Rev. Lett. **70**, 3816 (1993).
[4] M. Höhne, U. Juda, Yu. V. Martynov, T. Gregorkiewicz, C. A. J. Ammerlaan, and L. S. Vlasenko, Phys. Rev. B **49**, 13423 (1994).
[5] P. T. Huy and C. A. J. Ammerlaan, Phys. Rev. B **66**, 165219 (2002).
[6] C. Glover, M. E. Newton, P. Martineau, D. J. Twitchen, and J. M. Baker, Phys. Rev. Lett. **90**, 185507 (2003).
[7] E. M. Omeljanovsky, A. V. Pakhomov, and A. Y. Polyakov, Mater. Sci. Forum **38-41**, 1063 (1989).
[8] R. Bouanani-Rahbi, B. Clerjaud, B. Theys, A. Lemaître, and F. Jomard, Physica B (Amsterdam) **340-342**, 284 (2003).
[9] M. S. Brandt, S. T. B. Goennenwein, T. A. Wassner, F. Kohl, A. Lehner, H. Huebl, T. Graf, M. Stutzmann, A. Koeder, W. Schoch, and A. Waag, Appl. Phys. Lett. **84**, 2277 (2004).
[10] B. Clerjaud, D. Wasik, R. Bouanani-Rahbi, G. Strzelecka, A. Hruban, and M. Kaminska, J. Appl. Phys. **103**, 123507 (2008).
[11] S. T. B. Goennenwein, T. A. Wassner, H. Huebl, M. S. Brandt, J. B. Philipp, M. Opel, R. Gross, A. Koeder, W. Schoch, and A. Waag, Phys. Rev. Lett. **92**, 227202 (2004).
[12] C. Bihler, W. Schoch, W. Limmer, S. T. B. Goennenwein, and M. S. Brandt, Phys. Rev. B **79**, 045205 (2009).
[13] C. Bihler, M. Kraus, M. S. Brandt, S. T. B. Goennenwein, M. Opel, M. A. Scarpulla, R. Farshchi, D. M. Estrada, and O. Dubon, J. Appl. Phys. **104**, 013908 (2008).
[14] C. Bihler, G. Ciatto, H. Huebl, G. Martinez-Criado, P. J. Klar, K. Volz, W. Stolz, W. Schoch, W. Limmer, F. Filippone, A. Amore Bonapasta, and M. S. Brandt, Phys. Rev. B **78**, 235208 (2008).
[15] T. Graf, M. Gjukic, M. Hermann, M. S. Brandt, M. Stutzmann, L. Görgens, J. B. Philipp, and O. Ambacher, J. Appl. Phys. **93**, 9697 (2003).
[16] M. S. Brandt, N. M. Johnson, R. J. Molnar, R. Singh, and T. D. Moustakas, Appl. Phys. Lett. **64**, 2264 (1994).
[17] T. Graf, M. Gjukic, M. Hermann, M. S. Brandt, M. Stutzmann, and O. Ambacher, Phys. Rev. B **67**, 165215 (2003).
[18] D. J. Newman and B. Ng, Rep. Prog. Phys. **52**, 699 (1989).
[19] J. P. Perdew, K. Burke, and M. Ernzerhof, Phys. Rev. Lett. **78**, 1396 (1997).
[20] H. J. Monkhorst and J. D. Pack, Phys. Rev. B **13**, 5188 (1976).
[21] S. Blügel, H. Akai, R. Zeller, and P. H. Dederichs, Phys. Rev. B **35**, 3271 (1987).
[22] P. E. Blöchl, Phys. Rev. B **62**, 6158 (2000).
[23] C. J. Pickard and F. Mauri, Phys. Rev. B **63**, 245101 (2001).
[24] http://www.quantum-espresso.org
[25] S. G. Louie, S. Froyen, and M. L. Cohen, Phys. Rev. B **26**, 1738 (1982).
[26] U. Gerstmann, A. P. Seitsonen, and F. Mauri, Phys. Status Solidi B **245**, 924 (2008).
[27] H. J. Kulik, M. Cococcioni, D. A. Scherlis, and N. Marzari, Phys. Rev. Lett. **97**, 103001 (2006).
[28] S. Limpijumnong, J. E. Northrup, and C. G. Van de Walle, Phys. Rev. Lett. **87**, 205505 (2001).
[29] S. Limpijumnong, J. E. Northrup, and C. G. Van de Walle, Phys. Rev. B **68**, 075206 (2003).
[30] B. Clerjaud, D. Cote, A. Lebkiri, C. Naud, J. M. Baranowski, K. Pakula, D. Wasik, and T. Suski, Phys. Rev. B **61**, 8238 (2000).
[31] R. E. Watson and A. J. Freeman, *Hyperfine Interactions* (Academic, New York, 1967).
[32] S. J. C. H. M. van Gisbergen, M. Godlewski, T. Gregorkiewicz, and C. A. J. Ammerlaan, Phys. Rev. B **44**, 3012 (1991).
[33] U. Gerstmann, A. T. Blumenau, and H. Overhof, Phys. Rev. B **63**, 075204 (2001).
[34] S. Limpijumnong and C. G. Van de Walle, Phys. Rev. B **68**, 235203 (2003).
[35] W. Götz, N. M. Johnson, D. P. Bour, M. D. McCluskey, and E. E. Haller, Appl. Phys. Lett. **69**, 3725 (1996).
[36] A. Burchard, M. Deicher, D. Forkel-Wirth, E. E. Haller, R. Magerle, A. Prospero, A. Stötzler, and the ISOLDE-Collaboration, in *III-V Nitrides*, edited by F. A. Ponce, T. D. Moustakas, I. Akasaki, and B. A. Monemar, MRS Symposia Proceedings Vol. 449 (Materials Research Society, Warrendale, PA, 1997), p. 961.